

# Improvement of interfacial tension measurement using a captive bubble in conjunction with axisymmetric drop shape analysis (ADSA)

Y.Y. Zuo<sup>a</sup>, M. Ding<sup>b</sup>, A. Bateni<sup>a</sup>, M. Hoorfar<sup>a</sup>, A.W. Neumann<sup>a,\*</sup>

<sup>a</sup> Department of Mechanical and Industrial Engineering, University of Toronto, 5 King's College Road, Toronto, Ont., Canada M5S 3G8

<sup>b</sup> Division of Engineering Science, Faculty of Applied Science and Engineering, University of Toronto, 40 St. George Street, Toronto, Ont., Canada M5S 2E4

Received 22 December 2003; accepted 2 April 2004

Available online 21 September 2004

## Abstract

Axisymmetric drop shape analysis (ADSA) is a method to measure surface tension using drop or bubble profiles. Combining ADSA with a captive bubble configuration (ADSA-CB) facilitates pulmonary surfactant related studies. The accuracy of ADSA-CB is crucially dependent on the quality of the bubble profile extracted from the raw image. In the previous version of ADSA-CB, a global thresholding method was used to segment the bubble profile. However, that technique is of limited accuracy for images with noise and/or lack of contrast. In this paper, a new generation of ADSA-CB using the Canny edge detector was developed. To obtain better results, a novel edge smoothing technique, termed axisymmetric liquid fluid interfaces-smoothing (ALFI-S), was introduced and incorporated with the Canny edge detector to extract bubble profiles. The performance of the new version of ADSA-CB was evaluated using captive bubble images under different conditions. The results suggest that the new methodology is capable of producing accurate surface tension values under a variety of circumstances.

© 2004 Elsevier B.V. All rights reserved.

**Keywords:** Surface tension; Axisymmetric drop shape analysis (ADSA); Captive bubble; Canny edge detector; Axisymmetric liquid fluid interfaces-smoothing (ALFI-S)

## 1. Introduction

The determination of the surface tension at an air–liquid or liquid–liquid interface is of importance in a wide range of problems in pure and applied science. Many techniques have been developed to measure surface tension [1,2]. Among commonly used methods, drop shape methods offer a number of advantages as they require less sample, are applicable to both air–liquid and liquid–liquid interfaces, and are versatile and applicable to various situations, including extreme temperature and pressure [3].

Surface tension measurement using a drop shape method usually involves four steps. First, the image of a liquid drop or a gas bubble is acquired using a photographic or other image acquisition device. Second, the profile of the drop or the bubble is extracted from the raw image using an edge segmentation or detection operation. Usually, the edge detection step is followed by an edge smoothing procedure in which the outliers remaining in the extracted edge are removed using some edge smoothing technique. Finally, the smoothed edge coordinates [4] or some critical parameters associated with the drop (or bubble) geometry, e.g. the height and the diameter of the drop [5], are fed into a calculation scheme to compute surface tension.

Drop shape methods have been used in the captive bubble experiment. A captive bubble surfactometer (CBS) was

\* Corresponding author. Tel.: +1 416 978 1270; fax: +1 416 978 7753.  
E-mail address: neumann@mie.utoronto.ca (A.W. Neumann).

first introduced by Schürch et al. [6] to study the surface activity of pulmonary surfactant systems. Without contact of the bubble to any kind of support, CBS is able to provide a film-leakage-proof experimental environment. Without film leakage, an ultralow surface tension less than  $1 \text{ mJ/m}^2$  can be readily observed in a CBS [7]. In CBS, the captive bubble images taken in the experiments were enhanced by an image processing program and the bubble profiles were extracted by a simple thresholding method [8]. Edge smoothing was performed by manual editing. The bubble height ( $h$ ) and diameter ( $d$ ) were then measured from the bubble profile. Surface tension was calculated by substituting the ratio of bubble height to diameter ( $h/d$ ) into a polynomial modified from the formulas derived by Malcolm and Elliott [5].

Axisymmetric drop shape analysis (ADSA) is a surface tension measurement methodology first introduced by Rotenberg et al. [4] and has been significantly improved by del Río and Neumann [9]. In ADSA, surface tension of a bubble (or drop) profile is identified by the best fitted theoretical profile given by the classical Laplace equation of capillarity. Details of the mathematical calculations can be found elsewhere [4,9]. ADSA has been used to perform accurate measurement of surface tension in a variety of applications, including the studies of dynamic [10] and ultralow surface tension [11]. ADSA can be also used in conjunction with a pendent drop (ADSA-PD) [12] or a captive bubble (ADSA-CB) [13] configuration as a film balance to study insoluble films. As a film balance, ADSA-CB has been used to investigate the dynamic behavior of both adsorbed and spreading films. Lu et al. [14,15] used ADSA-CB to study lung surfactant and polymer enhanced lung surfactant films, which are adsorbed from the lung surfactant suspension. Pison and his colleagues [16,17] used ADSA-CB to study the surface dilatational properties, such as surface viscosity and elasticity, of dipalmitoylphosphatidylcholine (DPPC) and DPPC/protein films. By spreading DPPC inside the bubble, ADSA-CB was also used to study the interaction between the monolayer and the gas phase generated by evaporation of the spreading solvents [18].

As in CBS and several other methods [19–23], a thresholding method was employed in ADSA-CB to segment the bubble profile. Thresholding is a simple, non-contextual segmentation technique. A binary image composed of only black and white pixels is created from a grayscale image after performing thresholding. The implementation of thresholding segmentation was described in detail by Prokop et al. [13]. In brief, first, a rectangular area containing only the bubble as shown in Fig. 1(a) was determined as a working region by the user. Second, a histogram showing the intensity distribution in the working region was generated as shown in Fig. 1(c). The histogram shows two principal peaks, which represent the black bubble and the bright background. The peak representing the bubble is so narrow and high that it appears as a vertical line. A threshold value was determined by the average of these two principal peaks. Third, the image in the working region was scanned in both horizontal and vertical

directions until at least three consecutive pixels with the grey level less than the threshold value were found. The coordinates of the first of these points were then taken as the edge point (as shown in Fig. 1(e)). The success of thresholding critically depends on the selection of an appropriate threshold value [24]. However, determining an accurate threshold value is usually difficult. A histogram can be established a priori to help determine the threshold value. However, the histogram method suffers from two main restrictions [24]: (1) only a clean and fairly high contrast image can generate a histogram with two distinct peaks; (2) the application of histogram shape only works for foreground and background regions of similar total areas. Noisy images present a challenge to all drop shape techniques. In work involving pulmonary surfactant, the addition of water soluble, uncharged polymers such as polyethylene glycol (PEG) is of considerable biomedical interest [25–28]. Such polymers cause flocculation and hence a noisy image. A sample image of a captive bubble in a mixture of 0.5 mg/ml BLES (a typical exogenous lung surfactant, discussed in detail later) and 50 mg/ml PEG is shown in Fig. 1(b). Apart from the main object, the captive bubble, numerous small black spots are randomly distributed throughout the entire image. These black spots are believed to be the aggregates of phospholipids, created by a PEG-induced depletion force [29,30]. The presence of these large aggregates significantly increases the noise of the image, which makes the peak representing the background in the histogram quite small (see Fig. 1(d)). If two local maxima still exist in the histogram, it is found that the average of these two peaks, 110, cannot appropriately segment the bubble profile. The edge shown in Fig. 1(f) is obviously not the desired undisturbed smooth edge. That is, the histogram method to choose a threshold value fails for a noisy image such as that shown in Fig. 1(b).

When the histogram ceases to function, the determination of threshold becomes essentially subjective and random. In principle, any intensity value between the two principal peaks can be chosen as a threshold. However, an inappropriate threshold value can significantly distort the bubble profile, thus decreasing the accuracy and consistency of the surface tension measurement. This is due to the fact that surface tension measurements are extremely sensitive to the accuracy of the drop profile [31]. Prokop et al. [13] pointed out that the accuracy of surface tension measurement using thresholding is about one order of magnitude less than that of gradient methods. Such a reduced accuracy is intolerable for a precise surface tension measurement.

Therefore, the purpose of this paper is to find an edge detector that is robust against noise, to replace thresholding. The Canny edge detector was found to be the most suitable algorithm for extracting the bubble profiles from images on extensive conditions, including images with noise and/or lack of contrast. To obtain further improved results, a novel edge smoothing technique, termed axisymmetric liquid fluid interfaces-smoothing (ALFI-S), is also introduced. In addition, an optical distortion correction scheme is also

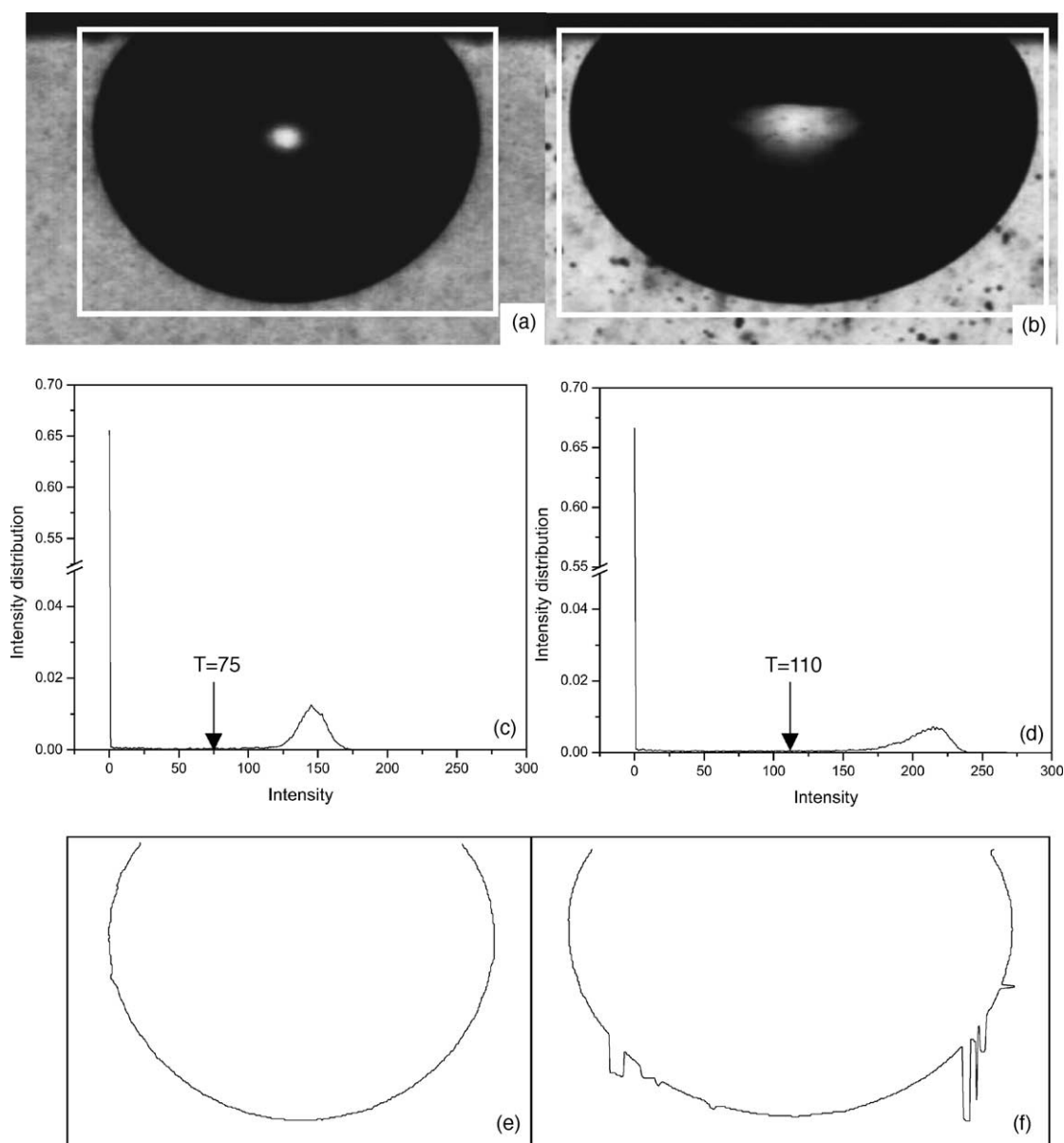


Fig. 1. Determining threshold value by using intensity histogram for both clean and noisy images. (a) A captive bubble in 0.5 mg/ml BLES. (b) A captive bubble in the mixture of 0.5 mg/ml BLES and 50 mg/ml PEG. (c) Histogram in the working region of (a). (d) Histogram in the working region of (b). (e) Successfully segmented edge of (a). (f) Unsuccessfully segmented edge of (b).

integrated into this calculation. Distilled water, lung surfactant suspensions at different concentrations, and mixtures of lung surfactant and PEG are used to generate typical captive bubble images with different amounts of noise and contrast. They are used to evaluate the performance of the new bubble analysis methodology.

## 2. Materials and methods

### 2.1. Materials

In order to test the new approach for images under various conditions, lung surfactant suspensions, mixtures

of lung surfactant and polymer, and water were used. Bovine lipid extract surfactant (BLES Biochemicals Inc., London, Ont., Canada) was prepared from bovine natural lung surfactant obtained by bronchopulmonary lavage with organic extraction. BLES contains about 98% phospholipids and 2% proteins. The protein components in BLES are only surfactant-associated proteins B (SP-B) and C (SP-C). High molecular weight hydrophilic proteins, SP-A and SP-D, were removed due to immunological concerns. BLES was stored frozen in sterilized vials with an initial concentration of 27 mg/ml. It was diluted to the desired concentration by 0.6% saline with 1.5 mM  $\text{CaCl}_2$  on the day of the experiment. Polyethylene glycol (PEG) (M.W. 10,000, Sigma, St. Louis, MO, USA) was used without

further purification. Dry PEG was added to the above diluted BLES in the desired concentration. The water used in the experiments was demineralised and doubly distilled.

## 2.2. Experimental set-up

The experimental set-up is shown in Fig. 2. The captive bubble chamber is made of stainless steel with two optical glass windows. Before the introduction of the bubble, the chamber was filled with approximately 1 ml liquid sample. The temperature inside the chamber was thermostatically controlled by a water bath (Model RTE-111, Neslab Instruments Inc., USA). An ultrafine thermocouple (AWG40, T type, Teflon insulated, Omega Eng. Inc., Laval, Quebec, Canada) was used to monitor the temperature in the chamber. After a temperature of 37 °C was reached and remained stable, an air bubble with a volume of about 20  $\mu\text{l}$  was injected into the chamber using a microsyringe (50  $\mu\text{l}$ , #1705, Gastight<sup>®</sup>, Hamilton Co., USA) through the side port of the chamber. The bubble rose and came to rest at the ceiling. The bubble was illuminated by a light source (Model V-WLP1000, Newport Corp., Fountain Valley, CA, USA) and bubble images can be acquired with a speed of up to 30 images per second. The image acquisition system consists of a microscope (Apozoom, Leitz Wetzlar, Germany), a CCD camera (Model 4815-5000, Cohu Co., USA) and a digital video processor (Parallax Graphics, CA, USA), which performs the frame grabbing and digitization of the image to 640 by 480 with 256 grey levels for each pixel where 0 represents black and 255 represents white. The acquired images were stored in a SUN workstation (Sparc Station-10, Sun Microsystems Inc., USA) for further analysis by the image processing program.

After each experiment, an image of a calibration grid pattern (square pattern with 0.25 mm spacing, Graticules Ltd., Tonbridge Kent, UK) on an optical glass was taken at the same position as the images of the captive bubble. The image of the grid was used for both correction of optical distortion (discussed later) and calibration. A scale factor was then calculated from the grid image to convert the coordinates of the bubble profile from pixels to millimeters. Usually one

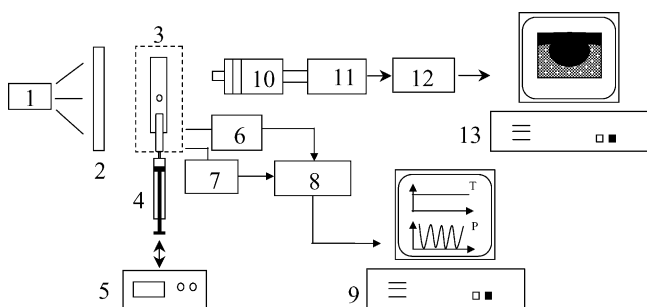


Fig. 2. Schematic of the captive bubble set-up. (1) Light source; (2) diffuser; (3) thermostated captive bubble chamber; (4) motor driven syringe; (5) motor controller; (6) thermocouple; (7) pressure transducer; (8) universal data acquisition card; (9) PC; (10) microscope; (11) CCD camera; (12) digital video processor; (13) workstation.

millimeter accounts for about 100 pixels in an image with a magnification of 10 and a resolution of 640  $\times$  480.

## 3. Image analysis

### 3.1. Detection of the bubble profile

#### 3.1.1. Selection of an appropriate edge detector

The edge in an image is characterized by a rapid change in some physical properties, such as intensity and reflectivity [32]. The general interest in the information associated with edges provoked the development of numerous edge detectors using a variety of algorithms. Due to the inherent attribute of an edge, i.e. discontinuity in the intensity, use of derivative algorithms is the most popular approach to the development of an edge detector [33]. Both the first and the second order derivatives are used in practice. The first order derivatives are usually obtained by using the gradient. Gradient edge detection is one of the earliest edge detection methods and measures the local maxima of the gradient across an edge. The pioneer gradient edge detectors include the Roberts operator, Prewitt operator, Sobel operator. The second order derivatives are usually implemented by using the Laplacian, in which edge points are located by finding the zero-crossings of the Laplacian, e.g. the so-called LoG edge detector.

The efficiency of the edge detectors can be significantly degraded by noise. Noise is an unexplained variation in intensity values [33]. It may be introduced into the image during the acquisition process from various sources. Some sources of the noise [34] are the uncertainty due to the electronic devices (e.g. uncertainties of the sensor, fluctuation in the light intensity, salt-and-pepper noise in signal transmission), blur due to drop evaporation and condensation, and ambiguity due to poor focus. For captive bubble images in lung surfactant related studies, another source of noise arises from the presence of large aggregates in the liquid phase surrounding the air-liquid interface. The existence of noise makes the detection of the bubble profile very difficult. Therefore, noise reduction plays a crucial role in analyzing captive bubble images.

Unfortunately, most of the traditional edge detectors, e.g. Sobel or LoG, are not robust against noise [35]. Promoted by the rapid development of computer science, most recent edge detectors are increasingly strong in eliminating noise. Their algorithms are based on optimal filters [36–39], fuzzy techniques [40], neural networks [41], discrete singular convolution algorithms (DSC) [42], and a number of others. An entropic edge detector [3,34] was reported to be applicable to detect a drop profile under any situation including images with different kinds of noise and/or lack of contrast. This entropic detector is based on the evaluation of Jensen-Shannon (JS) divergence [43], which is a measurement of the cohesion of a set of probability distributions having the same number of possible realizations. Combined with ADSA, the entropic edge detector performs well in the extraction of sessile and

pendent drop profiles from a noisy background, thereby offering more accurate surface tension and contact angle results [34]. However, an obvious drawback of this method is that it is very sensitive to the selection of user-specified parameters. This is due to the fact that only a few edge pixels can be detected directly because of the extreme conditions in which the algorithm has to work [34]. Therefore, a very high confidence level is required for these few edge pixels. This is done by setting up an optimal set of parameters. However, it is not straightforward to obtain this set since seven parameters are involved in this detector.

In order to find an appropriate edge detector for captive bubble images, three criteria are used: (1) The edge detector must be robust against noise; (2) It must be well-developed and broadly used in the field of computer vision; (3) The code must be readily available. Based on the above three criteria, algorithms by Canny [36] and Shen and Castan [37] are the most promising candidates. Both of them are based on optimal filters, making them strong in noise reduction. Conceptually, they are both composed of three operations: noise reduction, edge detection and localization, and false-edge suppression. The implementations of these two algorithms were obtained from [44]. Further modification has been made to enable the program to deal with different image formats.

Both Canny and Shen-Castan can produce optimal results under certain circumstances [44]. However, the performance of edge detectors cannot be compared straightforwardly since the comparison is dependent on several factors [45]: the algorithm itself, the tested images, the edge detector parameters, the criteria used, and, most importantly, the subsequent use of the detected edges [46]. Nguyen and Ziou [46] evaluated the performance of various edge detectors based on six well defined errors, i.e. omission, localization, multiple response, sensitivity, false-edge suppression and orientation errors. An edge detector exhibiting the least errors outperforms the others. The edge detectors used in the comparison include the Canny, the Shen-Castan and several others. The comparison suggests that the Canny operator has the lowest multiple-response, sensitivity, suppression and orientation errors while the Shen-Castan has higher errors in all of the above four categories, especially in the multiple-response and suppression errors. The poor multiple-response attribute of the Shen-Castan filter was also reported elsewhere [47]. However, the Shen-Castan operator has the lowest omission error and a better localization performance than the Canny dose. It was suggested that an edge detector with low multiple-response and sensitivity errors has a high omission error and vice versa [46]. The importance of these errors depends on the subsequent application of the detected edge. In ADSA-CB, the detected edge is fed into ADSA to calculate surface tension. It was suggested by Cheng et al. [31] that a smaller number of edge points with a higher accuracy can produce more precise ADSA results than a larger number of less accurate edge points. This is due to the fact that the ADSA calculation is based on non-linear least squares fitting of the experimental curve to the theoretical curves. Accordingly, the

existence of outliers can significantly distort the experimental curve, thus compromising the subsequent calculation. On the other hand, a slight discontinuity in the detected edge will not affect results much. It means that the multi-response and sensitivity errors are more deleterious than the omission error in the context of ADSA-CB. For the raw image shown in Fig. 1(b), the extracted bubble profile by means of the Canny and the Shen-Castan operators, is shown in Fig. 3(a) and (b), respectively. For both operators, a set of optimal parameters (discussed later) were used. As expected, the Shen-Castan operator detected more fine details in the raw image than the Canny did. However, most of these details absent in the Canny extracted edge are noise. Even if a subsequent edge smoothing procedure can help to eliminate some noise, an edge with less noise is still preferable. Consequently, the Canny edge operator is chosen for the new generation of ADSA-CB.

### 3.1.2. Canny edge detector

**3.1.2.1. Implementation.** The Canny edge detector [36] is a rigorously defined gradient edge operator and has been evaluated as a standard method to detect edges [45]. The popularity of the Canny edge detector is due to its three optimal criteria for performance evaluation: (1) Good detection: a detected edge should have a high probability matching the actual edge and low probability to report a false edge; (2) Good localization: the distance between the detected edge points and the actual edge points should be as small as possible; (3) Single response to an edge: a single edge should not cause a

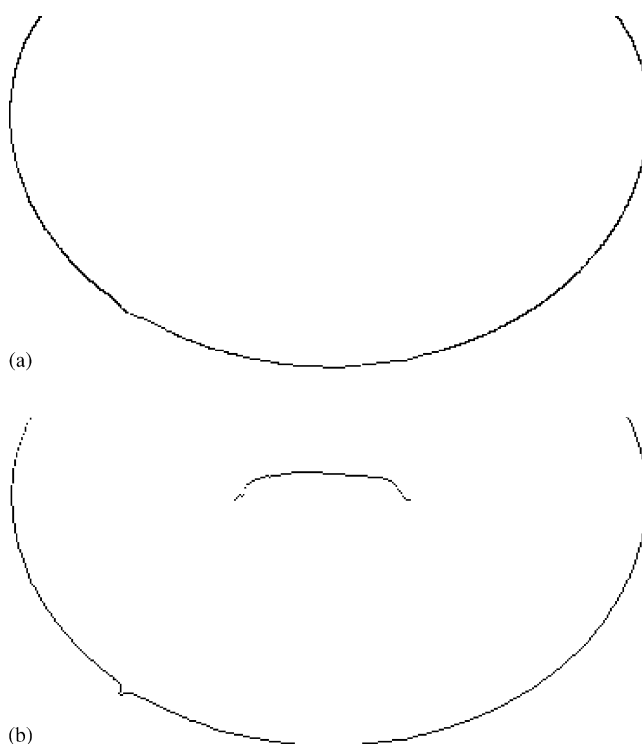


Fig. 3. Comparison of the bubble profile extracted from image shown in Fig. 1(b) by means of (a) Canny and (b) Shen-Castan edge detectors.

multiple-edge response. With these three criteria, Canny defined an optimal filter, which can be efficiently approximated by the first derivative of a Gaussian function. The smoothing step is followed by an optimal localization strategy; that is, the combination of non-maximum suppression and hysteresis thresholding.

In non-maximal suppression, a pixel with a gradient magnitude that is not a local maximum is removed and the edge is thinned down to only one pixel width. If the gradient magnitude at a pixel is larger than that at its two neighbors in the gradient direction, the pixel is marked as the edge. Otherwise, the pixel is marked as background.

To provide a more accurate and continuous edge, thresholding with hysteresis is performed subsequently. In hysteresis, thresholding is done by using two threshold values. If their magnitudes of gradient (edge strength) are above the higher threshold, the pixels in question constitute a definite edge. On the other hand, any pixels having edge strength less than the lower threshold are presumed not to be edge pixels. Any pixels adjacent to the edge pixels and having edge strengths greater than the lower threshold are also selected as edge pixels.

**3.1.2.2. Determination of optimal parameters.** The performance of an edge detector is dependent on the selection of the relevant parameters. Three user-specified parameters are involved in the Canny edge detector. They are the standard deviation ( $\sigma_G$ ) of the Gaussian filter, and the high ( $T_h$ ) and low ( $T_l$ ) threshold values used in the hysteresis thresholding operation. A systematic method was used by Heath et al. [48] to set up these parameters. Their method involves three steps: (1) a large number of combinations of these three parameters were proposed as candidates; (2) a subset of these parameters providing the best visual effect was picked up by a tester; (3) the final parameter set for each individual image was obtained from the subset using parameter selection experiments. Even though comprehensive, this method is not feasible in the processing of captive bubble images due to its complicated and time-consuming procedure.

To develop a straightforward parameter set-up procedure, one needs to investigate these three parameters further. The standard deviation  $\sigma_G$  controls the amount of smoothing. A Gaussian filter with a higher value of  $\sigma_G$  smoothes the image more. Consequently, the determination of  $\sigma_G$  depends on the characteristics of an image. A noisy image requires a larger value of  $\sigma_G$ . However, in practice, it is preferable to use a  $\sigma_G$  as small as possible provided that it can suppress noise adequately [49]. The reasons for that are: (1) larger values of  $\sigma_G$  smooth the noise more, but blur the edge more; (2) larger values of  $\sigma_G$  need a wider convolution mask, which significantly increases computation time; especially, when  $\sigma_G$  is greater than 4.0, the calculation time will conspicuously increase due to the dramatically increasing mask width. Therefore, the magnitude of  $\sigma_G$  could be generally chosen in the range of 0–4.0, depending on the characteristics of the image.

$T_h$  is a fraction of the gradient magnitude and  $T_l$  is a fraction of  $T_h$ . As a dominant parameter in hysteresis thresholding,  $T_h$  plays an important role in preserving the continuity of the detected edge. An inappropriately high  $T_h$  will suppress more edge points and therefore lead to a discontinuous edge.  $T_l$  can be calculated in the range of one third to one half of  $T_h$  [36].

The process to set up optimal parameters of the Canny edge detector is demonstrated in Fig. 4, as follows: (1) An initial value of  $\sigma_G$  is assigned as 1.0 for a clean image and 2.0 for a noisy image. (2)  $T_h$  is selected as 90%. That is, the edge strength represented by  $T_h$  is greater than that of 90% of the pixels studied.  $T_l$  is chosen as half of  $T_h$ . (3) The Canny edge detection is performed. (4) The quality of the detected edge is evaluated. If significant noise still remains in the extracted edge,  $\sigma_G$  is increased by 0.2; otherwise,  $\sigma_G$  is decreased by 0.2. Then, step 3 is repeated until a smooth edge is obtained by using the smallest  $\sigma_G$ . (5) After step 3, if a significant discontinuity exists in the extracted edge,  $T_h$  is decreased by 10%. Then, step 3 is repeated until there is no significant break in the extracted edge.

Actually, only  $\sigma_G$  needs to be determined manually in practice.  $T_h$  equal to the value of 90% and  $T_l$  equal to half of  $T_h$  are found to be adequate in most captive bubble images.

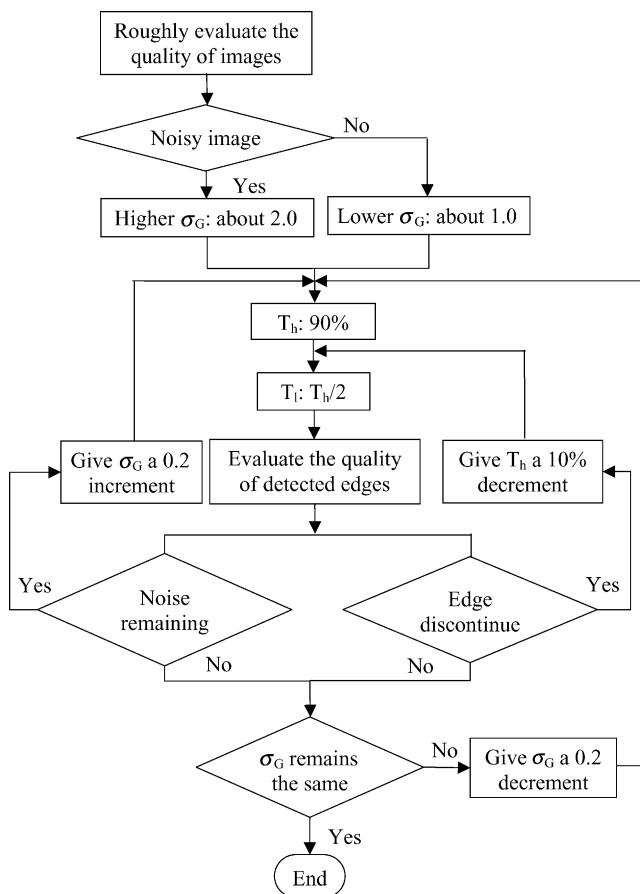


Fig. 4. Flow chart to set up optimal parameters for the Canny edge detector.

### 3.2. Smoothing of the bubble profile

Apart from the edge pixels, some outliers due to insufficient noise suppression can possibly exist after the edge detection. Considering the relative position of the outliers, they can be divided into two categories, i.e. outliers far away from the edge (isolated noise) and those close to the edge (adhering noise). There are two causes of isolated noise: particles in the suspension and the bright, central spot of the bubble due to refraction. The isolated noise can be readily removed by measuring cohesion. Any assumed edge pixel away from the main profile by 50 pixels (accounting for about 0.5 mm) is eliminated as isolated noise.

Adhering noise is mainly due to the dispersed particles adhering onto the bubble profile. Because of the adhesion to the bubble profile, eliminating adhering noise is more difficult than eliminating isolated noise. To do so, a specific edge smoothing technique needs to be used. Two edge smoothing methods, fifth order polynomial fitting (FOPF) and ALFI-S, are presented and compared in this paper. They share two common features. First, both methods are iteratively performed until no more noise points are found. Second, both methods use an adaptive criterion, i.e. three times the standard deviation ( $3\sigma$ ) to eliminate the noise. The standard deviation is calculated by comparing the experimental profile with the corresponding reference profile. The reference profile used in the so-called FOPF method involves a fifth order polynomial fitting while the best matched Laplacian curve is used in ALFI-S. With the assumption of a Gaussian distribution, the probability for an edge point out of the range of  $3\sigma$  is less than 0.27%. Hence, any assumed edge point with a deviation more than  $3\sigma$  from the reference profile can be safely eliminated as an outlier.

#### 3.2.1. FOPF method

The FOPF method was first introduced by Prokop et al. [13]. It has been further improved here by using the  $3\sigma$  criterion and an iterative procedure. FOPF was done by establishing a center of the bubble profile, calculating the distance from the center to each edge pixel and fitting of these distances to a fifth order polynomial. Then any point that was more than  $3\sigma$  away from the fitted polynomial was rejected as an outlier.

#### 3.2.2. ALFI-S method

ALFI-S is a novel edge smoothing technique based on the comparison of the experimental bubble (or drop) profile and the best fitted Laplacian curve. ALFI is a numerical method to generate theoretical bubble (or drop) profiles governed by the Laplace equation of capillarity, first introduced by del Río [50]. In ALFI-S, these theoretical profiles are fitted to the experimental edge points until the best match is found. As shown in Fig. 5, the best matched theoretical profile features a minimized objective function, which is defined as the sum of the squared normal distances ( $d_i$ ) between any experimental edge coordinates ( $X_i, Z_i$ ) and the Laplacian pro-

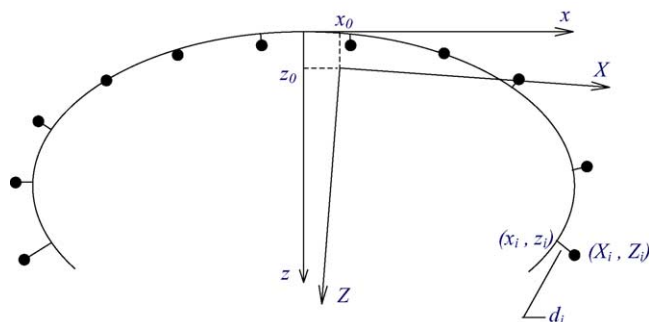


Fig. 5. Implementation of ALFI-S smoothing.

file coordinates ( $x_i, z_i$ ). Evaluating this objective function involves determining the minimum (normal) distance from the Laplacian curve to each experimental edge point. This is done using a one-dimensional Newton–Raphson iteration. Then, the standard deviation ( $\sigma$ ) can be evaluated from these normal distances and the  $3\sigma$  criterion can be used to eliminate outliers, just as FOPF does.

### 3.3. Correction of optical distortion

Images inevitably suffer, at least to some extent, from optical distortion due to the image acquisition hardware (microscope, camera and digital video processor). This distortion can cause major error in the surface tension result [31]. Therefore, correction of optical distortion is necessary for accurate surface tension measurement. The distortion correction scheme used in the current program was first implemented by Cheng [51] and modularized by Hoorfar [52]. The accuracy of this correction is  $\pm 1$  pixel [31,52].

### 3.4. Selection of the edge points

Two ways are commonly used to select edge points for the calculation in ADSA. One obvious way is to use all remaining points on the bubble profile after the edge detection and edge smoothing. Another approach is to use only a small fraction of randomly selected points along the profile and to repeat the procedure several times. The use of multiple calculations has been recommended in the past [31,53,54]. In this manner, the random errors introduced by the uncertainties of the edge coordinates would tend to average out. This strategy has the advantage that it provides a 95% confidence interval associated with each individual image. This strategy also uses less computer time. The number of smoothed edge points is around 700 for a bubble with a regular size. Running ADSA repeatedly with a small quantity of points reduces the total number of calculations, thus saving computer time. Using 20 randomly selected points 10 times was recommended by Cheng and Neumann [53]. Better accuracy can be obtained using 50 points at each calculation [9]. Therefore, a calculation scheme using 50 points 10 times is used at present, and will be compared to results obtained from the whole profile.

## 4. Results and discussion

### 4.1. Comparison of thresholding segmentation and Canny edge detection

Despite the fact that the performance of an edge detector is dependent on the relevant user-specified parameters, these parameters should not play a dominating role in the final results. That is, a desired image analysis algorithm should function properly with the least user-interference to avoid subjectivity and inconsistency.

Table 1 summarizes the dependence of surface tension measurements on the user-specified parameters, threshold value ( $T$ ) in thresholding and the standard deviation ( $\sigma_G$ ) of Gaussian filter used in the Canny edge detector. The calculations are based on the image shown in Fig. 1(b). For the sake of comparison, both calculations are performed using all of the edge points without correcting optical distortion.

As mentioned before, the histogram method is the only tool to provide a proper threshold value. However, it fails for a noisy image. When the histogram ceases to function, any intensity value between the two principal peaks, in principle, can be selected as a threshold. The first two columns in Table 1 show the surface tension measurements as a function of the threshold values. The threshold values are selected from 20 to 160, within the range of the two principal peaks (0 and 220) shown in Fig. 1(d). When the threshold value is increased to 160, surface tension results unreasonably deviate, which indicates that ADSA fails at such a high threshold value. The reason for this failure is apparent from the cor-

responding histogram shown in Fig. 1(d). It is noticed that the threshold, as it increases to 160, starts to enter the region of the intensity peak representing the background. A threshold in this region cannot separate the bubble profile from the background, thereby leading to the failure of ADSA. It is also noticed that within the range of 20–140, even though seemingly consistent surface tension results can be obtained, there is a clear trend in the results. With increasing threshold, the surface tension values increase by about 3%. It appears that the surface tension measurement using thresholding can depend somewhat on the user-specified parameter.

The last two columns in Table 1 show the parameter dependence of the Canny edge detector. Here, only the potentially sensitive parameter,  $\sigma_G$ , is studied, while  $T_h$  is selected as 90% and  $T_l$  is chosen as half of  $T_h$ . When  $\sigma_G$  is as low as 0.8, too many noise pixels remain in the extracted edge. ADSA fails for such a noisy edge. It is clear that in a quite large range of  $\sigma_G$ , from 1.0 to 4.0, the surface tension results are very consistent and there is no apparent trend. The 95% confidence interval associated with the mean value using the Canny edge detector is one order of magnitude less than that using thresholding. Apparently the Canny edge detector is not sensitive to the user-specified parameter.

### 4.2. Comparison of FOPF and ALFI-S methods

To compare the performance of FOPF and ALFI-S, a typical image as shown in Fig. 6 is analyzed. The tested image shows a captive bubble in a mixture of 0.5 mg/ml BLES and 50 mg/ml PEG. Thus in Fig. 6, four types of noise may be detected. They are: (a) isolated noise due to the bright, central spot; (b) isolated noise due to the particles dispersed in the liquid; (c) adhering noise due to a minor bubble resting against the ceiling; and (d) adhering noise due to the dark particles sticking to the bubble. Noise due to suspended particles is inevitable in certain practical applications, including lung surfactant preparations. The interruption due

Table 1

Dependence of surface tension values on the user-specified parameters: threshold value ( $T$ ) in thresholding and standard deviation ( $\sigma_G$ ) of the Gaussian filter in the Canny edge detector

Thresholding		Canny edge detector	
$T$	Surface tension (mJ/m <sup>2</sup> )	$\sigma_G$	Surface tension (mJ/m <sup>2</sup> )
20	23.08	0.8	Failed
40	23.30	1.0	23.65
60	23.28	1.2	23.68
80	23.58	1.4	23.74
100	23.64	1.6	23.74
120	23.80	1.8	23.74
140	23.74	2.0	23.72
160	Failed	2.2	23.70
–	–	2.4	23.70
–	–	2.6	23.70
–	–	2.8	23.64
–	–	3.0	23.63
–	–	3.2	23.64
–	–	3.4	23.63
–	–	3.6	23.64
–	–	3.8	23.64
–	–	4.0	23.64
Mean	$23.49 \pm 6.4 \times 10^{-3}$	Mean	$23.68 \pm 6.7 \times 10^{-4}$

The calculations are based on the image shown in Fig. 1(b) without correction of optical distortion, using the whole profile. The mean values are shown with 95% confidence intervals.

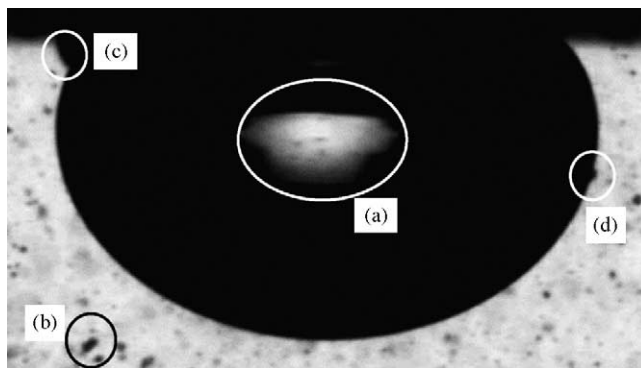


Fig. 6. A sample image showing typical noise in a captive bubble image. The liquid is a mixture of 0.5 mg/ml BLES and 50 mg/ml PEG. There are four types of noise: (a) isolated noise due to refraction; (b) isolated noise due to dark particles; (c) adhering noise due to a minor bubble; (d) adhering noise due to black particles.

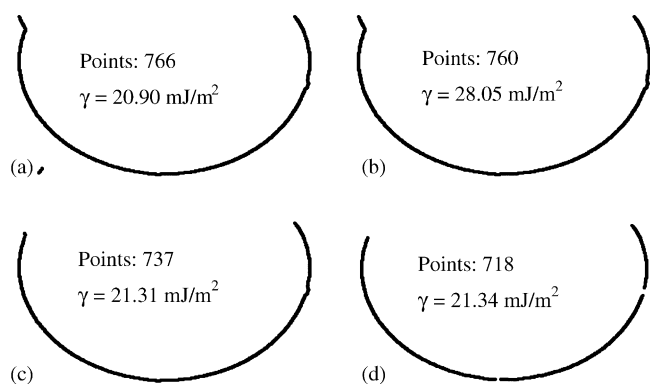


Fig. 7. Effect of edge smoothing techniques. (a) Edge right after the Canny edge detection. (b) Edge after eliminating isolated noise. (c) Edge after eliminating adhering noise using FOPF. (d) Edge after eliminating adhering noise using ALFI-S.

to the minor bubble is also common in practice especially when the bubble is studied under dynamic conditions.

The extracted bubble profile right after the Canny edge detection is shown in Fig. 7(a). There are 766 edge points in Fig. 7(a) including isolated and adhering noise due to particles and adhering noise due to the small bubble. Without deleting any noise points a surface tension of 20.90 mJ/m<sup>2</sup> would be calculated. The isolated noise can be readily removed by measuring cohesion of the edge pixels. As shown in Fig. 7(b), 6 points accounting for the isolated noise have been eliminated. The surface tension value jumps to 28.05 mJ/m<sup>2</sup>. To further remove the adhering noise, both FOPF and ALFI-S methods are employed respectively. The smoothed edges using FOPF and ALFI-S are shown in Fig. 7(c) and (d). The remaining edge points after FOPF and ALFI-S are 737 and 718, respectively, and the corresponding surface tension values are 21.31 and 21.24 mJ/m<sup>2</sup>. It is clear that both FOPF and ALFI-S can effectively smooth the edge and yield similar surface tension measurement. The surface tension measurements with and without edge smoothing can cause deviation as high as 7 mJ/m<sup>2</sup> for this particular image. Obviously edge smoothing in such situations is a necessity.

Table 2 shows the iterative process for FOPF and ALFI-S. The iteration repeats four times for FOPF and eight times for ALFI-S. Close scrutiny shows that the effect of each iteration

is not dependent on how many points are eliminated but on where the eliminated points are located. As shown in Table 2, after the first iteration, the surface tension value jumps dramatically towards the final result. Even if more noise points were removed in the subsequent iterations (e.g. the 2nd, 3rd, and 4th iteration of ALFI-S), the surface tension values do not change considerably. This is due to the fact that the first iteration removes most noise points due to the minor bubble close to the ceiling. It suggests that the accuracy of edge points close to the ceiling plays a crucial role in determining surface tension. This finding is in line with previous studies on sessile drops [31,50,53]. Cheng et al. [31,53] and del Río [50] suggested that the surface tension measurement is critically sensitive to the accuracy of edge points close to the solid–liquid interface for a sessile drop. However, it is not sensitive to the shape near the apex since the shape there is nearly spherical, independent of the interfacial tension. Therefore, even though ALFI-S outperforms FOPF in removing finer adhering noise around the apex and the right side of the bubble, the surface tension values from the two smoothing methods are quite similar.

#### 4.3. Analysis of sample images

Six images of captive bubbles are selected as samples to evaluate the performance of the Canny edge detector and the edge smoothing techniques. The six images are chosen to represent a wide variety of conditions of noise and contrast. Each image contains a single captive bubble in the central portion of the image. Each captive bubble rests against the ceiling of the chamber and is surrounded by some liquid. As shown in Fig. 8, the liquids are: (a) distilled water; (b) 0.5 mg/ml BLES; (c) 0.5 mg/ml BLES + 30 mg/ml PEG; (d) 0.5 mg/ml natural surfactant; (e) 1.0 mg/ml BLES + 50 mg/ml PEG; (f) 0.8 mg/ml BLES + 27 mg/ml PEG. Except for the first image, which was taken at 20 °C, the others were at 37 °C. In Fig. 8, the first two images represent clean images free of noise. (c) and (d) represent images with extensive noise. The noise in the natural surfactant is due to the SP-A induced large surfactant aggregates (LAs). Different from BLES, natural surfactant contains SP-A, which plays an important role in maintaining LAs in vitro [55]. As a result, the captive bubble

Table 2

Comparison of iterations of two edge smoothing techniques, FOPF (fifth order polynomial fitting) and ALFI-S (axisymmetric liquid fluid interfaces-smoothing)

Iteration	FOPF			ALFI-S		
	Eliminated points	Remaining points	Surface tension (mJ/m <sup>2</sup> )	Eliminated points	Remaining points	Surface tension (mJ/m <sup>2</sup> )
0	0	760	28.05	0	760	28.05
1	15	745	21.99	8	752	22.22
2	6	739	21.43	10	742	21.33
3	2	737	21.31	10	732	21.36
4	0	737	21.31	9	723	21.34
5	–	–	–	3	720	21.33
6	–	–	–	1	719	21.33
7	–	–	–	1	718	21.34
8	–	–	–	0	718	21.34

Edge smoothing was performed after eliminating the isolated noise as shown in Fig. 7(b).

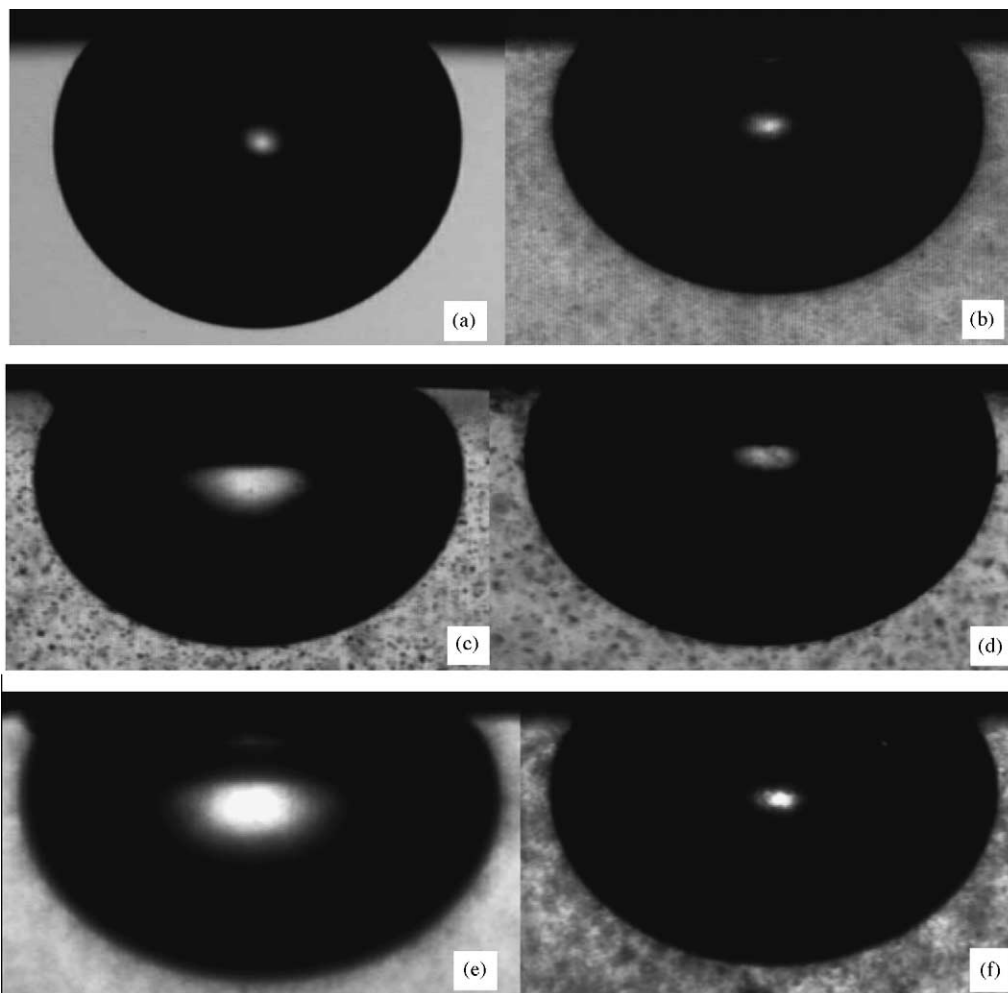


Fig. 8. Six sample images of captive bubbles in different liquids. They are: (a) distilled water; (b) 0.5 mg/ml BLES; (c) 0.5 mg/ml BLES + 30 mg/ml PEG; (d) 0.5 mg/ml natural lung surfactant; (e) 1 mg/ml BLES + 50 mg/ml PEG; (f) 0.8 mg/ml BLES + 27 mg/ml PEG.

image shown in Fig. 8(b) exhibits a much cleaner background than that of Fig. 8(d) even though the phospholipid concentrations are the same. Image (e) is a sample lacking contrast and (f) features both poor contrast and noise. The poor contrast is due to optical limitations because lung surfactant suspensions become murky at relatively high concentrations. For a captive bubble chamber with a capacity of 1.0 ml, a phospholipid concentration of 1–2 mg/ml was reported as the maximum concentration at which experiments can be conducted [56]. The extracted edges right after performing the Canny edge detection are shown in Fig. 9. Optimal parameters obtained by the procedure shown in Fig. 4 are used for all of the analyses. The values of  $\sigma_G$  are listed in Tables 3 and 4.

Even if some noise points still exist, the Canny edge detector successfully extracts all edges. A general edge consists of about 700–800 edge points. For the clean images shown in Fig. 8(a) and (b), the extracted edges are very smooth. For the noisy and low contrast images, satisfactory edges are also obtained. The broken edge shown in Fig. 9(d) is due to the non-uniform distribution of intensity in the raw image. Even though there is a deficiency on the left side, the right

side of the edge is completely preserved. Since the bubble profile is assumed to be axisymmetric, one side of the bubble profile is adequate for ADSA calculation as long as that side is complete and accurate. The isolated and adhering noise shown in Fig. 9 can be removed by separate procedures, as explained above. Using FOPF as well ALFI-S, smoothed edges are shown in Figs. 10 and 11, respectively. It is noticed that both FOPF and ALFI-S yield smooth edges for most cases. However, two points need to be stressed. First, ALFI-S is superior to FOPF in removing any fine noise, e.g. small bumps in Fig. 9(c)–(e). If the bumps are located around the ceiling, as in Fig. 9(c) and (e), a significant difference in surface tension value is expected from these two smoothing methods. Second, for edges shown in Fig. 9(f), FOPF fails because too many edge points (more than 400) are deleted. This may be due to the assumption that FOPF assumes that the distance from each smoothed edge point to the center of the bubble can be matched to a fifth order polynomial. To examine this assumption, a “perfect” curve representing the distances from the bubble center is calculated by means of ALFI with a given surface tension of 25 mJ/m<sup>2</sup> and a curvature of 4.0 cm<sup>-1</sup> at

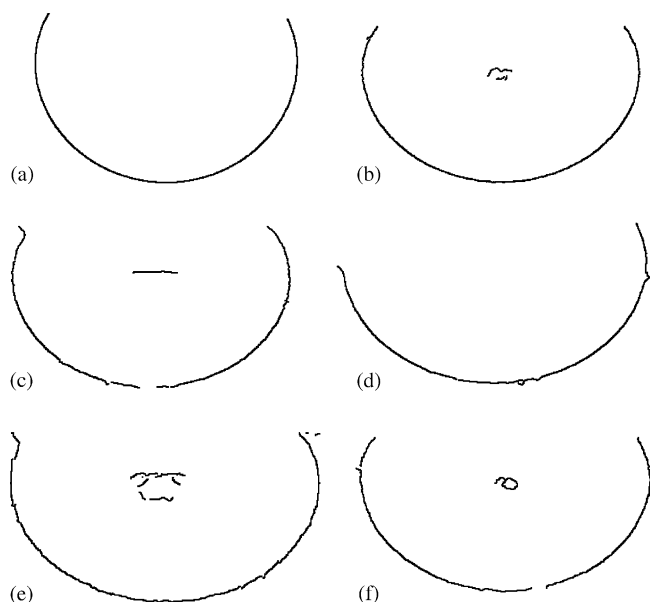


Fig. 9. Extracted edges from images shown in Fig. 8 right after the Canny edge detection. The detected numbers of edge points are: (a) 776; (b) 739; (c) 705; (d) 737; (e) 826; (f) 726.

the apex of the bubble, then fitted to polynomials of different order. The comparisons between the “perfect” curve and the corresponding polynomials are shown in Fig. 12. It is noted that the fifth order polynomial is not perfectly fitted to the theoretical curve and not necessarily better than the polynomials with fourth or sixth order. Especially edge pixels around the apex of the bubble (the middle region of *x*-coordinate in Fig. 12) exhibit a poor fit to the polynomials. Thus, FOPF works in many cases because these points are less critical than points near the ceiling. The unreasonable break in the smoothed edge shown in Fig. 10(f) may be due to this weakness of FOPF. Overall, it is apparent that ALFI-S is preferable to FOPF.

Table 3  
Surface tension measurements (mJ/m<sup>2</sup>) using FOPF (fifth order polynomial fitting) in conjunction with the Canny edge detector for images shown in Fig. 8

Image	$\sigma_G^a$	WP – DC <sup>b</sup>	WP + DC <sup>c</sup>	50 × 10 – DC <sup>d</sup>	50 × 10 + DC <sup>e</sup>
a	0.4	72.94	73.03	72.38 ± 0.90	72.98 ± 1.01
b	1.4	28.69	29.26	29.07 ± 0.34	29.61 ± 0.36
c	3.6	26.09	26.85	25.69 ± 0.37	26.44 ± 0.32
d	3.0	28.37	28.16	28.44 ± 0.33	28.35 ± 0.80
e	1.4	24.06	23.98	23.62 ± 0.20	23.76 ± 0.27
f	3.2			Failed	

<sup>a</sup> The standard deviation of the Gaussian filter used in the Canny edge detector.

<sup>b</sup> Calculation using the whole profile (WP) without optical distortion correction (DC).

<sup>c</sup> Calculation using the whole profile with optical distortion correction.

<sup>d</sup> Calculation using randomly selected 50 points 10 times without optical distortion correction.

<sup>e</sup> Calculation using randomly selected 50 points 10 times with optical distortion correction.

Table 4  
Surface tension measurements (mJ/m<sup>2</sup>) using ALFI-S (axisymmetric liquid fluid interfaces-smoothing) in conjunction with the Canny edge detector for images shown in Fig. 8

Image	$\sigma_G^a$	WP – DC <sup>b</sup>	WP + DC <sup>c</sup>	50 × 10 – DC <sup>d</sup>	50 × 10 + DC <sup>e</sup>
a	0.4	72.78	72.89	72.26 ± 1.11	73.17 ± 0.91
b	1.4	28.63	29.23	28.58 ± 0.42	29.62 ± 0.32
c	3.6	25.73	26.55	25.55 ± 0.18	26.34 ± 0.28
d	3.0	28.17	27.97	27.86 ± 0.24	27.88 ± 0.31
e	1.4	23.65	23.56	23.56 ± 0.21	23.75 ± 0.24
f	3.2	24.53	25.03	24.36 ± 0.34	24.91 ± 0.29

<sup>a</sup> The standard deviation of the Gaussian filter used in the Canny edge detector.

<sup>b</sup> Calculation using the whole profile (WP) without optical distortion correction (DC).

<sup>c</sup> Calculation using the whole profile with optical distortion correction.

<sup>d</sup> Calculation using randomly selected 50 points 10 times without optical distortion correction.

<sup>e</sup> Calculation using randomly selected 50 points 10 times with optical distortion correction.

The surface tension measurements for images shown in Fig. 8 are summarized in Table 3 for FOPF and in Table 4 for ALFI-S. The analysis of each edge is performed in four ways. They are: (1) calculation using the whole profile without optical distortion correction (WP – DC); (2) calculation using the whole profile with optical distortion correction (WP + DC); (3) calculation using 50 randomly selected edge points 10 times without optical distortion correction (50 × 10 – DC); (4) calculation using 50 randomly selected edge points 10 times with optical distortion correction (50 × 10 + DC). The values of surface tension calculated using randomly selected points are shown with the 95% confidence intervals.

As seen in Table 3, ADSA fails for image (f) when FOPF is used. However, a reasonable result can be obtained with

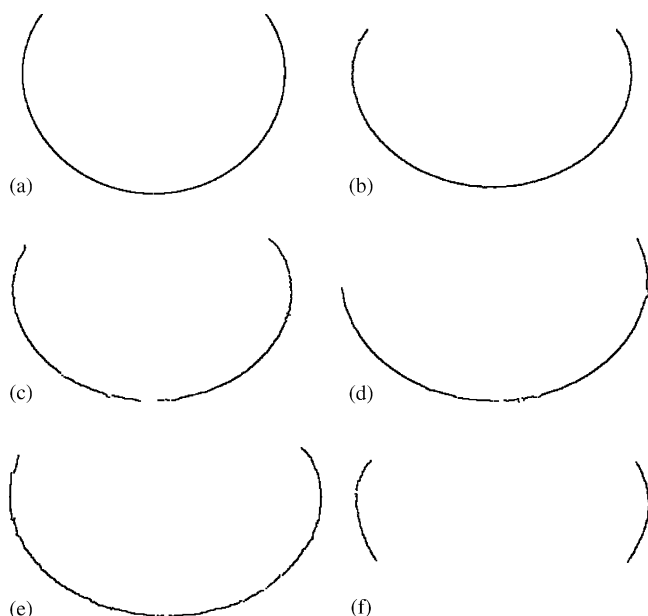


Fig. 10. Smoothed edges after removing isolated noise and adhering noise using FOPF. The remaining numbers of edge points are: (a) 757; (b) 731; (c) 690; (d) 698; (e) 754; (f) 301.

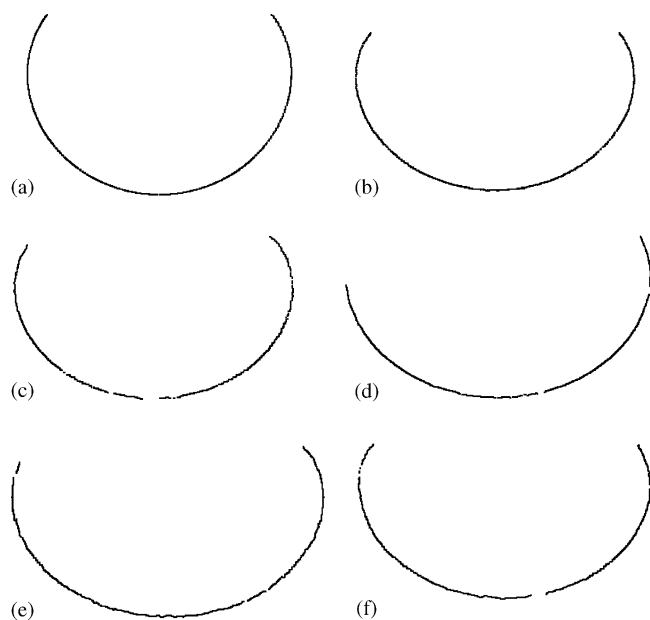


Fig. 11. Smoothed edges after removing isolated noise and adhering noise using ALFI-S. The remaining numbers of edge points are: (a) 742; (b) 724; (c) 667; (d) 683; (e) 756; (f) 700.

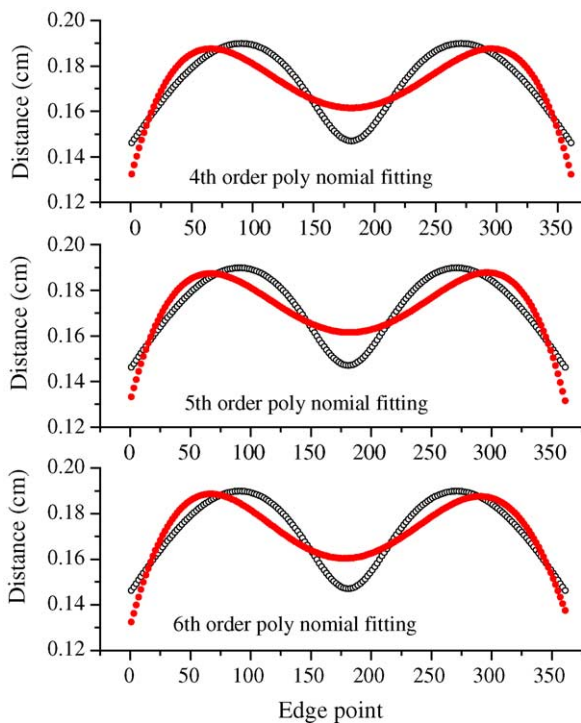


Fig. 12. Comparison of a “perfect” curve generated by axisymmetric liquid fluid interfaces (ALFI) to a series of polynomials with different order. The input of ALFI are a surface tension of  $25 \text{ mJ/m}^2$  and a curvature of  $4.0 \text{ cm}^{-1}$  at the apex of the bubble. The “perfect” curve is generated by calculating the distances from the center of the bubble to each edge point. Edge points are numbered from the left to the right along the bubble profile. Open symbols represent points on the “perfect” curve and solid symbols represent the corresponding polynomials.

ALFI-S. The failure of FOPF (Fig. 10(f)) is due to the absence of edge points around the apex of the bubble so that a suitable initial estimate of the surface tension cannot be established. Except for this case, the surface tension measurements using these two methods are quite similar for each image.

Another common concern is computer time. This was tested for FOPF and ALFI-S on a PC with a 2.0 GHz CPU. It is found that FOPF is generally two times faster than ALFI-S. However, even for ALFI-S, the computational time is always less than 2 s for different images. Therefore, ALFI-S should be used in general. Only if the computational time is limited, a combination of FOPF and ALFI-S is recommended. FOPF can be used first to take the advantage of its fast implementation. If it fails or produces unreasonable results, ALFI-S can be used subsequently.

#### 4.4. Validation of the new method using water

The accuracy of the experimental results depends essentially only on the quality of the experimental coordinate points and is not limited by ADSA [53]. Therefore, accurate surface tension measurements are anticipated using the Canny edge detector in conjunction with ALFI-S. To validate the precision of the new methodology, surface tension is measured in distilled water at  $20^\circ\text{C}$ . Twenty images of a stationary captive bubble were taken within 10 s at a uniform interval of 0.5 s. The first of these 20 images is shown in Fig. 8(a). Table 5 shows the surface tension measurements for these 20 images. One more significant figure is deliberately kept in the mean values to demonstrate the accuracy of the method.

The mean values of the results calculated using the four different strategies are similar. However, it is noticed that the 95% confidence intervals associated with the mean values using randomly selected points are about three to four times greater than those using the whole profile. Use of the whole profile produces a higher accuracy. It was not generally recommended in previous work simply due to the computer time required. However, the issue of computer time has become relatively unimportant in view of the rapid development and availability of high power computers. Therefore, a calculation using the whole profile is recommended for accurate surface tension measurement.

Another inference from Table 5 is that the effect of optical distortion correction on the surface tension values seems to be much less than reported previously [31]. However, the previous conclusion was based on the pendant drop configuration. Probably the geometrical arrangement of a captive bubble is not as sensitive to optical distortion as that of a pendant drop. A detailed investigation on the distortion correction algorithm is beyond the scope of this paper. Literature values for the surface tension of water at  $20^\circ\text{C}$  are given as  $72.75 \text{ mJ/m}^2$  in [57] and  $72.88 \text{ mJ/m}^2$  in [58]. As it stands, it is not possible to conclude that the distortion correction improves the result when considering the whole profile, as one of the two mean values agrees perfectly with one literature value

Table 5  
Surface tension measurements ( $\text{mJ/m}^2$ ) of distilled water at  $20^\circ\text{C}$

Bubble no.	WP – DC <sup>a</sup>	WP + DC <sup>b</sup>	$50 \times 10 - \text{DC}^c$	$50 \times 10 + \text{DC}^d$
1	72.78	72.89	$72.26 \pm 1.11$	$73.17 \pm 0.91$
2	72.80	72.91	$73.75 \pm 1.60$	$73.28 \pm 0.81$
3	72.75	72.86	$72.05 \pm 1.29$	$72.19 \pm 1.42$
4	72.92	73.04	$73.38 \pm 1.13$	$73.74 \pm 1.42$
5	72.85	72.97	$73.41 \pm 1.19$	$72.69 \pm 1.11$
6	72.91	73.02	$73.67 \pm 0.65$	$73.28 \pm 0.77$
7	72.53	72.63	$71.20 \pm 0.71$	$72.75 \pm 1.67$
8	72.53	72.64	$72.09 \pm 1.16$	$73.22 \pm 1.28$
9	72.76	72.85	$72.37 \pm 0.76$	$73.54 \pm 1.49$
10	72.87	72.99	$73.14 \pm 1.53$	$73.19 \pm 0.76$
11	72.36	72.46	$72.68 \pm 1.54$	$72.59 \pm 0.64$
12	72.52	72.63	$72.01 \pm 1.08$	$72.79 \pm 1.05$
13	72.69	72.79	$73.42 \pm 1.30$	$72.58 \pm 0.99$
14	72.64	72.75	$74.42 \pm 1.32$	$72.95 \pm 1.72$
15	72.85	72.99	$73.38 \pm 1.44$	$74.02 \pm 0.97$
16	72.58	72.69	$73.95 \pm 1.19$	$72.16 \pm 1.58$
17	73.07	73.13	$73.06 \pm 1.20$	$72.09 \pm 1.01$
18	72.87	72.97	$73.82 \pm 1.38$	$72.32 \pm 1.15$
19	72.88	72.99	$73.55 \pm 1.34$	$72.45 \pm 0.92$
20	72.94	72.94	$73.05 \pm 1.32$	$72.94 \pm 0.85$
Mean	$72.755 \pm 0.003$	$72.857 \pm 0.002$	$72.984 \pm 0.010$	$72.897 \pm 0.008$

Images of a static bubble were taken in sequence with an interval of 0.5 s. Canny edge detector and ALFI-S were used in the edge detection and edge smoothing steps, respectively. The error limits with 95% confidence intervals.

<sup>a</sup> Calculation using the whole profile (WP) without optical distortion correction (DC).

<sup>b</sup> Calculation using the whole profile with optical distortion correction.

<sup>c</sup> Calculation using randomly selected 50 points 10 times without optical distortion correction.

<sup>d</sup> Calculation using randomly selected 50 points 10 times with optical distortion correction.

and the other one with the second literature value. However, when randomly selected points (50 points 10 times) are used for calculation, a notable improvement in surface tension result ( $\sim 0.1 \text{ mJ/m}^2$ ) is obtained due to the use of the correction, as the mean value without distortion correction is clearly too high. Be that as it may, it is apparent that the captive bubble arrangement can produce very accurate surface tension results when bubble images are processed by the combination of ADSA with the Canny edge detection and smoothing of the experimental profile. Nevertheless, it is worth to point out that, even though much more precise, the surface tension values still fluctuate within a range of  $0.5 \text{ mJ/m}^2$ . For a rigorous measurement of pure liquids, therefore, the use of a pendant drop arrangement is preferable, which is known to produce more accurate results.

## 5. Summary

The Canny edge detector was found to outperform thresholding for extracting edges from a captive bubble image. The combination of the Canny edge detector and ADSA allows accurate and consistent surface tension measurements from captive bubble experiments. To achieve an undisturbed bubble profile, edge smoothing is necessary following the edge detection. Two categories of noise, isolated noise and adhering noise, were defined. To remove these two types of noise, different approaches have to be used. First, iso-

lated noise can be readily removed by application of a cohesion criterion to the edge points. Then, the adhering noise can be removed using specific edge smoothing techniques. Two edge smoothing techniques, FOPF and ALFI-S, were introduced and compared. The comparison showed that ALFI-S is superior to FOPF with respect to accuracy and stability while FOPF requires less computation time. As this latter aspect is not severe in most applications, ALFI-S is generally recommended for all users. For cases where computer time is indeed crucial, a combination of FOPF and ALFI-S can be employed taking advantages of the fast speed of FOPF as well as the reliable performance of ALFI-S.

The analysis of a series of sample images showed that ALFI-S in conjunction with the Canny edge detector is capable of extracting edges from captive images under various conditions, including images with extensive noise, poor contrast, or non-uniform lighting conditions. As a result, accurate surface tension values can be obtained since the measurement is essentially only dependent on the quality of the edge. To validate the new methodology, surface tension measurements were performed with distilled water at  $20^\circ\text{C}$ . The results are in a good agreement with the literature value.

Finally, the two strategies using the whole profile or randomly selected points repeatedly were compared. Best results are obtained when using the whole profile. The effect of optical distortion correction seems to be not as important to a captive bubble as to a pendant drop.

## Acknowledgements

This work was supported by a grant from the Canadian Institute of Health Research (MOP-38037) and an Open Fellowship from University of Toronto for YYZ. We also thank Dr. David Bjarneson of BLES Biochemicals Inc. for his generous donation of the BLES samples.

## References

- [1] A.W. Adamson, *Physical Chemistry of Surfaces*, 5th ed., Wiley, New York, 1990.
- [2] A.W. Neumann, R.J. Good, *Surface and Colloid Science*, Plenum Press, New York, 1979.
- [3] J.A. Holgado-Terriza, J.F. Gómez-Lopera, P.L. Luque-Escamilla, C. Atae-Allah, M.A. Cabrerizo-Vilchez, *Coll. Surf. A: Physicochem. Eng. Aspects* 156 (1999) 579.
- [4] Y. Rotenberg, L. Boruvka, A.W. Neumann, *J. Coll. Interf. Sci.* 93 (1983) 169.
- [5] J.D. Malcolm, C.D. Elliott, *Can. J. Chem. Eng.* 58 (1980) 151.
- [6] S. Schürch, H. Bachofen, J. Goerke, F. Possmayer, *J. Appl. Physiol.* 67 (1989) 2389.
- [7] G. Putz, J. Gerke, S. Schürch, J.A. Clements, *J. Appl. Physiol.* 76 (1994) 1417.
- [8] W.M. Schoel, S. Schürch, J. Goerke, *Biochim. Biophys. Acta* 1200 (1994) 281.
- [9] O.I. del Río, A.W. Neumann, *J. Coll. Interf. Sci.* 196 (1997) 136.
- [10] D.Y. Kwok, M.A. Cabrerizo-Vilchez, Y. Gomez, S.S. Susnar, O.I. del Río, D. Vollhardt, R. Miller, A.W. Neumann, *Dynamic Properties of Interfaces and Association Structures*, AOCs Press, Champaign, IL, 1996. Chapter 14.
- [11] D.Y. Kwok, P. Chiefalo, B. Khorshiddoust, S. Lahooti, M.A. Cabrerizo-Vilchez, O. del Río, A.W. Neumann, in: R. Sharma (Ed.), *Surfactant Adsorption and Surface Solubilization*, ACS volume, ACS Series 615, Washington, DC, 1995, Chapter 24.
- [12] D.Y. Kwok, D. Vollhardt, R. Miller, D. Li, A.W. Neumann, *Coll. Surf. A: Physicochem. Eng. Aspects* 88 (1994) 51.
- [13] R.M. Prokop, A. Jyoti, M. Eslamian, A. Garg, M. Mihaila, O.I. del Río, S.S. Susnar, Z. Policova, A.W. Neumann, *Coll. Surf. A: Physicochem. Eng. Aspects* 131 (1998) 231.
- [14] J. Lu, J. Distefano, K. Philips, P. Chen, A.W. Neumann, *Respir. Physiol.* 115 (1999) 55.
- [15] J.J. Lu, W.W.Y. Cheung, L.M.Y. Yu, Z. Policova, D. Li, M.L. Hair, A.W. Neumann, *Respir. Physiol. Neurobiol.* 130 (2002) 69.
- [16] N. Wüstneck, R. Wüstneck, V.B. Fainerman, R. Miller, U. Pison, *Coll. Surf. B* 21 (2001) 191.
- [17] N. Wüstneck, R. Wüstneck, U. Pison, *Langmuir* 19 (2003) 7521.
- [18] R. Wüstneck, N. Wüstneck, D. Vollhardt, R. Miller, U. Pison, *Mater. Sci. Eng. C* 8/9 (1999) 57.
- [19] H.J.J. Girault, D.J. Schiffrin, B.D.V. Smith, *J. Electr. Chem.* 137 (1982) 207.
- [20] H.J.J. Girault, D.J. Schiffrin, B.D.V. Smith, *J. Coll. Interf. Sci.* 101 (1984) 257.
- [21] S.H. Anastasiadis, J.K. Chen, J.T. Koberstein, A.F. Siegel, J.E. Sohn, J.A. Emerson, *J. Coll. Interf. Sci.* 119 (1989) 55.
- [22] S.Y. Lin, K. McKeigue, C. Maldarelli, *AIChE J.* 36 (1990) 1785.
- [23] F.K. Hansen, G. Rodsrud, *J. Coll. Interf. Sci.* 141 (1991) 1.
- [24] M. Seul, L. O’Gorman, M.J. Sammom, *Practical Algorithms for Image Analysis, Description, Examples, and Code*, Cambridge University Press, New York, 1999.
- [25] H.W. Tausch, K.W. Lu, J. Goerke, J.A. Clements, *Am. J. Respir. Crit. Care Med.* 159 (1999) 1391.
- [26] K.W. Lu, H.W. Tausch, B. Robertson, J. Goerke, J.A. Clements, *Am. J. Respir. Crit. Care Med.* 162 (2000) 623.
- [27] K.W. Lu, H.W. Tausch, B. Robertson, J. Goerke, J.A. Clements, *Am. J. Respir. Crit. Care Med.* 164 (2001) 1531.
- [28] H. Campbell, K. Bosma, A. Brackenbury, L. McCaig, L.J. Yao, R. Veldhuizen, J. Lewis, *Am. J. Respir. Crit. Care Med.* 165 (2002) 475.
- [29] T. Kuhl, Y. Guo, J.L. Alderfer, A.D. Berman, D. Leckband, J. Israelachvili, S.W. Hui, *Langmuir* 12 (1996) 3003.
- [30] D. Meyuhos, S. Nir, D. Lichtenberg, *Biophys. J.* 71 (1996) 2602.
- [31] P. Cheng, D. Li, L. Boruvka, Y. Rotenberg, A.W. Neumann, *Coll. Surf.* 43 (1990) 151.
- [32] W.K. Pratt, *Digital Image Processing: PIKS Inside*, 3rd ed., Wiley, 2001.
- [33] R.C. Gonzalez, R.E. Woods, *Digital Image Processing*, 2nd ed., Prentice-Hall, Upper Saddle River, NJ, 2002.
- [34] C. Atae-Allah, M.A. Cabrerizo-Vilchez, J.F. Gómez-Lopera, J.A. Holgado-Terriza, R. Román-Roldán, P.L. Luque-Escamilla, *Meas. Sci. Technol.* 12 (2001) 288.
- [35] P. Qiu, S.M. Bhandarkar, *Pattern Recogn. Lett.* 17 (1996) 849.
- [36] J. Canny, *IEEE Trans. Pattern Anal. Mach. Intell.* 8 (1986) 679.
- [37] J. Shen, S. Castan, *CVGIP: Graphical Models and Image Processing* 54 (1992) 112.
- [38] R.A. Boie, I. Cox, P. Rehak, *Proceedings of the IEEE Conference on Computer Vision and Pattern Recognition*, 1986, p. 100.
- [39] R.A. Boie, I. Cox, *Proceedings of the IEEE First International Conference on Computer Vision*, 1987, p. 450.
- [40] T. Kimura, A. Taguchi, Y. Murata, *Electronics and Communications in Japan*, Part 3 83 (1) (2000) 61.
- [41] H.S. Wong, T. Caelli, L. Guan, *Pattern Recogn.* 33 (2000) 427.
- [42] Z.J. Hou, G.W. Wei, *Pattern Recogn.* 35 (2002) 1559.
- [43] J.F. Gómez-Lopera, J. Martínez-Aroza, A.M. Robles-Pérez, R. Román-Roldán, *J. Math. Imaging Vision* 13 (2000) 35.
- [44] J.R. Parker, *Algorithms for Image Processing and Computer Vision*, Wiley Computer Pub., 1997.
- [45] M.D. Heath, S. Sarkar, T. Sanocki, K.W. Bowyer, *Comput. Vision Image Understanding* 69 (1) (1998) 38.
- [46] T.B. Nguyen, D. Ziou, *Pattern Recogn. Lett.* 21 (2000) 805.
- [47] D. Demigny, T. Kamlé, *IEEE Trans. Pattern Anal. Mach. Intell.* 19 (11) (1997) 1199.
- [48] M.D. Heath, S. Sarkar, T. Sanocki, K.W. Bowyer, *IEEE Trans. Pattern Anal. Mach. Intell.* 19 (12) (1997) 1338.
- [49] D. Ziou, A. Koukam, *Pattern Recogn.* 31 (1998) 587.
- [50] O.I. del Río, M.A.Sc. Thesis, University of Toronto, 1993.
- [51] P. Cheng, Ph.D. Thesis, University of Toronto, 1990.
- [52] M. Hoorfar, A.W. Neumann, *Axisymmetric Drop Shape Analysis (ADSA) for the determination of surface tension and contact angle*, *J. Adhesion* 80 (2004) 727.
- [53] P. Cheng, A.W. Neumann, *Coll. Surf.* 62 (1992) 297.
- [54] R.M. Prokop, O.I. del Río, N. Niyakan, A.W. Neumann, *Can. J. Chem. Eng.* 74 (1996) 534.
- [55] R.A.W. Veldhuizen, L.J. Yao, S.A. Hearn, F. Possmayer, J.F. Lewis, *Biochem. J.* 313 (1996) 835.
- [56] S. Schürch, F.H.Y. Green, H. Bachofen, *Biochim. Biophys. Acta* 1408 (1998) 180.
- [57] N.B. Vargaftik, B.N. Volkov, L.D. Voljak, *J. Phys. Chem. Ref. Data* 12 (1983) 817.
- [58] J.J. Jasper, *J. Phys. Chem. Ref. Data.* 1 (1972) 841.